Quantitative Elemental Mapping at Atomic Resolution Using X-Ray Spectroscopy

G. Kothleitner,[1] M. J. Neish,[2] N. R. Lugg,[2] S. D. Findlay,[3] W. Grogger,[1] F. Hofer,[1] and L. J. Allen[2]
[1]Institute for Electron Microscopy and Nanoanalysis, Graz University of Technology, Steyrergasse 17, 8010 Graz, Austria and Centre for Electron Microscopy, Steyrergasse 17, 8010 Graz, Austria
[2]School of Physics, University of Melbourne, Parkville, Victoria 3010, Australia
[3]School of Physics, Monash University, Clayton, Victoria 3800, Australia
(Received 15 November 2013; published 26 February 2014)

Elemental mapping using energy-dispersive x-ray spectroscopy in scanning transmission electron microscopy, a well-established technique for precision elemental concentration analysis at submicron resolution, was first demonstrated at atomic resolution in 2010. However, to date atomic resolution elemental maps have only been interpreted qualitatively because the elastic and thermal scattering of the electron probe confounds quantitative analysis. Accounting for this scattering, we present absolute scale quantitative comparisons between experiment and quantum mechanical calculations for both energy dispersive x-ray and electron energy-loss spectroscopy using off-axis reference measurements. The relative merits of removing the scattering effects from the experimental data against comparison with direct simulations are explored.

DOI: 10.1103/PhysRevLett.112.085501 PACS numbers: 61.05.jd, 68.37.Ma, 78.70.En

Given a condensed matter sample, where the atoms are, what the atoms are, and how they are bonded are fundamental questions permeating all modern materials characterization and analysis. Two complementary tools that have been developed to address precisely these questions are atomic resolution elemental mapping via electron energy loss spectroscopy (EELS) [1–4] and, more recently, energy dispersive x-ray (EDX) analysis [5–8] in scanning transmission electron microscopy (STEM). Both offer the advantage of elemental specificity over the long-established method of high-angle annular dark field (HAADF) imaging. Quantification, a critical ingredient for structural and chemical nanocharacterization of advanced materials, has recently been achieved in atomic resolution HAADF STEM through absolute scale comparison with simulations [9–11]. By contrast, despite significant recent progress [12], absolute scale quantification of EELS images remains elusive. The effective inelastic interaction underlying EDX mapping is more localized than that for EELS, and EDX images should thus be more readily interpretable, but factors such as fluorescence yields, x-ray absorption, and detector geometry make absolute scale quantification in EDX more challenging [13,14].

At lower resolutions, off-axis conditions are sought because multiple scattering of the electron probe along aligned atomic columns ("channeling") produces a nonlinear relation between signal and composition [15,16]. But this is seldom desirable at atomic resolution, where the structures of interest are only clearly interpretable when atomic columns are aligned along the beam direction. For thin specimens, Lu *et al.* [17] used EDX analysis to quantitatively assess composition variation across an interface based on the object function approximation, where the image is regarded as a convolution of the probe intensity with an object structure function. However, for thicker specimens, which are often used to increase EDX count rates, the effect of the elastic and thermal scattering of the probe means that the object function approximation breaks down. For instance, simulations have shown a notable thickness variation in the ratio of EDX signals between columns with identical concentrations of an element of interest but differing concentrations of other elements [18]. Comparison with simulation offers a way of interpreting and correcting for scattering effects, but the multiplicity of poorly known factors is such that absolute scale quantification still eludes us. For that, a standard of reference is needed. Kotula *et al.* [19] endeavored to calibrate atomic resolution EDX maps from the data itself via the image averaged signal, a robust quantity independent of both coherent and incoherent lens aberrations [20]. However, this quantity is not immune to the influence of channeling. In this Letter, we explore the use of a "nonchanneling" (off axis) signal to calibrate atomic resolution STEM EDX and EELS images for quantitative analysis.

Figure 1 shows EDX, EELS, and HAADF STEM images of a $SrTiO_3$ specimen, viewed in the $\langle 001 \rangle$ orientation, which were simultaneously acquired on an FEI Titan 80-300 at an accelerating voltage of 300 kV with a Super-X x-ray detector and a Gatan Quantum ERS DualEELS spectrometer. The images are 50×50 pixels, each pixel representing 0.07 $Å^2$. The STEM probe was corrected for third order spherical aberration and the probe forming aperture semiangle was 20 mrad. The collection semiangle at the spectrometer was 41 mrad. The EDX detector spanned 0.7 sr. The acquisition time for a single

 © 2014 American Physical Society

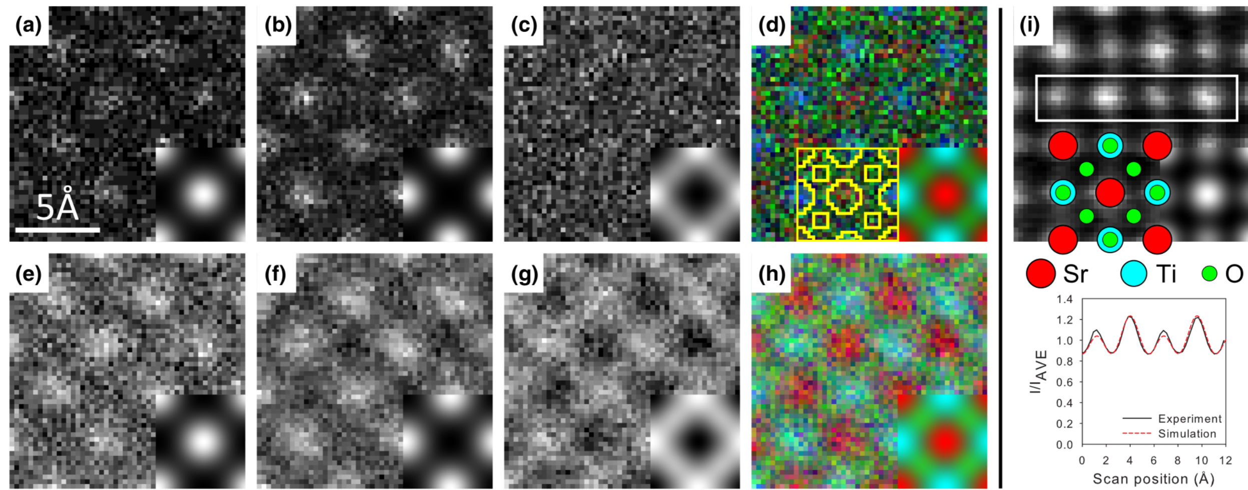

FIG. 1. (Color online) (color online). Experimental atomic resolution EDX elemental maps for the ⟨001⟩ direction in $SrTiO_3$ for the (a) Sr K shell, (b) Ti K shell, (c) O K shell, and (d) color composite (Sr red, Ti blue, O green). Overlaid on (d) are the mask areas over which the signal will be integrated. Simultaneously acquired EELS maps for the (e) Sr $L_{2,3}$ edge, (f) Ti $L_{2,3}$ edge, (g) O K edge, and (h) color composite. (i) Simultaneously acquired HAADF image, with the projected averaged linescan over the boxed region shown below. Simulations, assuming a Gaussian incoherent effective source with a HWHM of 0.8 Å, are inset in each figure.

x-ray spectrum (one pixel) was 10 ms (corrected for dead time). With this new analytical hardware configuration [21], we discuss how EDX and EELS signals can be used to derive absolute volumetric concentrations (i.e., atomic number densities).

EDX elemental maps for the Sr K shell, Ti K shell, and O K shell are shown in Figs. 1(a)–(c), and combined in a color composite in Fig. 1(d). Simultaneously acquired EELS elemental maps for the Sr $L_{2,3}$, Ti $L_{2,3}$, and O K edges are shown in Figs. 1(e)–(g), and combined in a color composite in Fig. 1(h). Background subtraction was based on multiple-least-squares fitting, incorporating multiple scattering, and integration windows of 100 eV from threshold were used. Depending on the element, the signal-to-noise ratio is 2 to 8 times higher for the EELS data than the EDX data. The simultaneously acquired HAADF image is shown in Fig. 1(i). Simulations, inset on the images, were carried out in the quantum excitation of phonons (QEP) model [22] and assumed a thickness of 61 nm. This was determined within an estimated error of 5% from the mean free path for inelastic scattering into the detector [23] as calibrated on a focused ion beam milled rodlike specimen. An effective source size of Gaussian form with 0.8 Å half width half maximum—determined by good agreement with the HAADF image—is assumed.

After collecting the data shown in Fig. 1, the sample was tilted a few (less than 5) degrees off axis and the same measurements repeated. Care was taken to ensure that the specimen thickness, beam current, and recording time were identical between the two experiments. Assuming the off-axis experiment constitutes a "nonchanneling" condition, the EDX and EELS signals should be proportional to the atomic number density in the material [13]. For EDX, the proportionality constant will include such factors as the ionization cross section, the fluorescence yield, the specimen thickness, the x-ray absorption, the detector collection angle, the detector efficiency, and the dose. Since the structure of $SrTiO_3$ is known, the proportionality factors between the true atomic number density and the measured signals can be determined. After using these factors to convert each on-axis image in Fig. 1 to atomic number density units, the contributions from the vicinity of the Sr columns, Ti/O columns, and O columns were obtained using the masks indicated in Fig. 1(d), whose size was guided by the simulations—approximately 50% of the signal around a column is included in the area surrounding each column. Table I summarizes this analysis. The signal outside of these masks (denoted "elsewhere") and the full image signal are also given. By comparing these results to the known values (denoted "reference") it is clear that elastic and thermal scattering render misleading atomic concentrations.

Averaged over the full image, the effects of elastic and thermal scattering and the delocalization of the particular ionization edge can produce apparent number densities either larger or smaller than the actual values. It is also worth noting that oxygen vacancies are possible in strontium titanate which may make some small difference to the overall results and, in particular, would reduce the oxygen signal. The spatial variation is also revealing. In particular, there is a substantial contribution to all signals from columns which do not contain the element in question. Encountering a similar result, Kotula *et al.* [19] chose to subtract a "noncolumn-specific background" prior to attempting quantification. This approach has been used in HAADF imaging to some success [24], but has not been

TABLE I. Apparent atomic number densities (atoms per nm^3) as defined by integrating over the masks for the Sr, Ti/O, O columns shown in Fig. 1(d), "elsewhere" (i.e., the area outside all masks), and the full image. The experimental data were normalized using the off-axis calibration experiment. Reference values are from the known structure of $SrTiO_3$. Inversion values are those obtained after the effects of channeling and thermal diffuse scattering have been removed from the data.

Area	Sr		Ti		O	
	EDX	EELS	EDX	EELS	EDX	EELS
Sr column	45	32	27	11	40	29
Ti/O column	19	16	65	19	47	58
O column	20	18	26	12	39	48
Elsewhere	25	20	31	14	50	45
Full image	27	21	34	14	49	44
Reference	16.8	16.8	16.8	16.8	50.4	50.4
Inversion	21.0	⋯	22.8	⋯	45.3	⋯

rigorously justified and moreover has proven unnecessary when detailed simulations are performed in conjunction with a well-characterized experiment [9–11]. That the O K shell EDX signal on the Sr columns is almost equal to that on the pure O columns should not be interpreted to mean that the O concentration in these two columns is similar, but rather that, as a consequence of the elastic and thermal scattering of the electron probe, the electron probe can trigger about the same number of O K shell ionization events regardless of which of these two columns it is positioned upon.

Channeling, then, is the confounding factor, which we seek to overcome using simulation. An inversion procedure which deconvolves the multiple elastic and thermal scattering of the probe from the experimental data was recently presented in the context of EELS spectrum imaging [25,26], and can equally be applied to STEM EDX data. It produces an effective scattering potential analogous to the "object" in the object function model used by Lu *et al.* [17]. The inversion procedure makes fewer assumptions than a direct simulation: both assume the structure for determining the scattering of the probe, but the inversion procedure does not presuppose the form of the EDX effective scattering potentials. Applying the inversion procedure to the present data, the effective scattering potential obtained for the Sr K shell is shown in Fig. 2(a). As inverse problems are often ill-conditioned and sensitive to small changes in the input, we regularize our conjugate gradient least squares (CGLS) approach to the inversion by selecting the iteration number where the results have stabilized, which is achieved after eight iterations [Fig. 2(b)], an approach which is justified in Ref. [27]. Subsequent to the inversion, i.e., having removed the effects of channeling, our revised estimate for the atomic number density of Sr is 21 atoms/nm^3. This differs somewhat from the known value of 16.8 atoms/nm^3, but not by nearly so much as if we chose to simply use the on-axis image mean signal (27 atoms/nm^3). The inversion results for the other EDX images are included in Table I.

The inversion procedure was not applied to the EELS images as it assumes the effective interaction potential to be local, which is not true in EELS unless the collection aperture is much larger than that used here.

The asymmetry and weak between-Sr-column signal in the effective scattering potential in Fig. 2 are attributed to the noisy input data. The deviation from the ideal atomic number density will also be influenced by uncertainties in parameters such as thickness, defocus, and spatial incoherence. Another approach to robust comparison is to compare the image average signal between experiment and simulation. This presupposes an adequate description of the effective scattering potential for EDX but is immune to

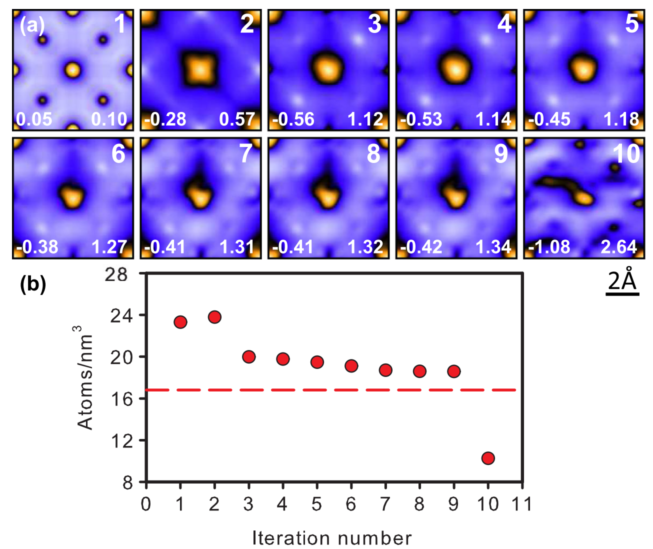

FIG. 2. (Color online) (color online). (a) Effective EDX signal scattering potential of the Sr K shell as a function of CGLS iteration number (1–10). Maxima and minima, in units such that integrating over the field of view and multiplying the thickness yields a density, are indicated on each subfigure. (b) Atomic density obtained for each iteration number (dashed line: nominal value). Convergence is achieved in the region of 7–9 iterations and deteriorates due to noise thereafter.

TABLE II. Apparent atomic number densities (atoms per nm^3) defined as in Table 1 save that now the experimental data have been renormalized such that the full image value is identical to that in the simulation.

Area	Sr				Ti				O			
	EDX		EELS		EDX		EELS		EDX		EELS	
	Ex. renorm.	Th.	Ex. renorm.	Th.	Ex. renorm.	Th.	Ex. renorm.	Th.	Ex. renorm.	Th.	Ex. renorm.	Th.
Sr column	39.3	39.1	26.2	26.3	22.6	16.3	13.5	12.8	48.2	49.4	32.8	42.5
Ti/O column	16.6	15.3	13.1	11.2	54.5	53.2	23.3	25.7	56.7	68.5	65.6	56.1
O column	17.5	19.0	14.7	14.8	21.8	20.7	14.7	15.4	47.0	61.6	54.4	52.4
Elsewhere	22.6	21.9	16.6	15.6	26.4	25.5	17.1	17.3	61.7	58.7	49.4	50.5
Full image	23.6	23.6	17.2	17.2	28.5	28.5	17.2	17.2	59.1	59.1	49.8	49.8
Reference	16.8	16.8	16.8	16.8	16.8	16.8	16.8	16.8	50.4	50.4	50.4	50.4
Inversion	18.4	···	···	···	19.1	···	···	···	54.5	···	···	···

uncertainties in the coherent and incoherent aberrations [20]. Allowing that some of the discrepancy in the inversion analysis above arose because the off-axis reference does not realize an ideal "nonchanneling" condition, we now renormalize the experimental data such that its full image mean precisely matches that of the simulation (which is itself normalized by reference to an ideal "nonchanneling" simulation). Table II shows a repetition of the mask analysis applied to the direct simulations inset in Fig. 1 and the renormalized experimental data. Though the renormalization forfeits absolute scale quantification, the good agreement between the column values, and the improved agreement of the postinversion results with the known values, show that the spatial variation in the images is quantitatively well described by our simulations. This agreement supports the hypothesis that the off-axis experimental reference used in our initial analysis was not completely immune to channeling. This suggests that, when seeking absolute scale normalization, particular care should be taken to obtain an experimental off-axis reference from an orientation that minimizes channeling effects (as assessed, for instance, by structure in a HAADF image). Alternatively, one could use an on-axis experiment for a region of known thickness, corrected for channeling effects via the inversion procedure described, as the reference against which a further experiment at a different thickness or in an uncharacterized portion of the sample is to be compared.

As our data demonstrate, atomic resolution features in spectroscopic STEM images do not necessarily imply column-by-column analysis, particularly from thicker specimens with x rays originating deep into the crystal where the electron probe has largely spread off the column on which it began. However, by accounting for the elastic and thermal scattering of the probe, we have shown that quantitative comparisons between experiment and theory using energy dispersive x-ray spectroscopy are possible, paving the way for quantitative atomic resolution EDX elemental mapping.

In this Letter we have used a specimen of known structure, which circumstance will perforce pertain to the initial calibration on a known reference specimen needed to determine the conversion factors underpinning quantitative analysis. In general, where less will be known about the structure of specimens of interest, an iterative strategy could be employed to obtain the structure. For example, in the first instance the inversion procedure could be applied taking into account only the position of the probe (but not its elastic or thermal scattering) to obtain an estimate for the inelastic scattering potential for the effective ionization potential pertinent to EELS or EDX. The information thus obtained could be used to generate a better estimate for the structure to seed the next iteration. A simultaneously acquired HAADF image could also provide a better starting point for such a procedure.

This research has received funding from the European Union within the 7th Framework Programme [FP7/2007-2013] under Grant Agreement no. 312483 (ESTEEM2) and was also supported under the Discovery Projects funding scheme of the Australian Research Council (Projects No. DP140102538 and No. DP110102228). The substantial help of Bernd Kraus, Paul Thomas, and Ray Twesten from Gatan, as well as Meiken Falke and Ralf Terborg from Bruker, in setting up this particular analytical hardware configuration is acknowledged.

[1] M. Bosman, V. J. Keast, J. L. Garcia-Munoz, A. J. D'Alfonso, S. D. Findlay, and L. J. Allen, Phys. Rev. Lett. **99**, 086102 (2007).
[2] K. Kimoto, T. Asaka, T. Nagai, M. Saito, Y. Matsui, and K. Ishizuka, Nature (London) **450**, 702 (2007).
[3] D. A. Muller, L. Fitting Kourkoutis, M. Murfitt, J. H. Song, H. Y. Hwang, J. Silcox, N. Dellby, and O. L. Krivanek, Science **319**, 1073 (2008).
[4] P. Wang, A. J. D'Alfonso, S. D. Findlay, L. J. Allen, and A. L. Bleloch, Phys. Rev. Lett. **101**, 236102 (2008).
[5] A. J. D'Alfonso, B. Freitag, D. Klenov, and L. J. Allen, Phys. Rev. B **81**, 100101(R) (2010).
[6] M.-W. Chu, S. C. Liou, C.-P. Chang, F.-S. Choa, and C. H. Chen, Phys. Rev. Lett. **104**, 196101 (2010).

[7] D. O. Klenov and M. O. Zide, Appl. Phys. Lett. **99**, 141904 (2011).
[8] L. J. Allen, A. J. D'Alfonso, B. Freitag, and D. Klenov, MRS Bull. **37**, 47 (2012).
[9] J. M. LeBeau, S. D. Findlay, L. J. Allen, and S. Stemmer, Phys. Rev. Lett. **100**, 206101 (2008).
[10] A. Rosenauer, K. Gries, K. Müller, A. Pretorius, M. Schowalter, A. Avramescu, K. Engl, and S. Lutgen, Ultramicroscopy **109**, 1171 (2009).
[11] C. Dwyer, C. Maunders, C. L. Zheng, M. Weyland, P. C. Tiemeijer, and J. Etheridge, Appl. Phys. Lett. **100**, 191915 (2012).
[12] H. L. Xin, C. Dwyer, and D. A. Muller, Ultramicroscopy, doi: 10.1016/j.ultramic.2014.01.006 (2014).
[13] J. I. Goldstein, D. B. Williams, and G. Cliff, *Principles of Analytical Electron Microscopy*, edited by D. C. Joy, A. D. Romig, and J. I. Goldstein (Plenum Press, New York, 1986), pp. 155–217.
[14] M. Watanabe and D. B. Williams, J. Microsc. **221**, 89 (2006).
[15] M. Watanabe, D. W. Ackland, A. Burrows, C. J. Kiely, D. B. Williams, O. L. Krivanek, N. Dellby, M. F. Murfitt, and Z. Szilagyi, Microsc. Microanal. **12**, 515 (2006).
[16] F. Meisenkothen, R. Wheeler, M. D. Uchic, R. D. Kerns, and F. J. Scheltens, Microsc. Microanal. **15**, 83 (2009).
[17] P. Lu, J. Xiong, M. Van Benthem, and Q. Jia, Appl. Phys. Lett. **102**, 173111 (2013).
[18] B. D. Forbes, A. J. D'Alfonso, R. E. A. Williams, R. Srinivasan, H. L. Fraser, D. W. McComb, B. Freitag, D. O. Klenov, and L. J. Allen Phys. Rev. B **86**, 024108 (2012).
[19] P. G. Kotula, D. O. Klenov, and H. S. von Harrach, Microsc. Microanal. **18**, 691 (2012).
[20] J. M. LeBeau, S. D. Findlay, L. J. Allen, and S. Stemmer, Ultramicroscopy **110**, 118 (2010).
[21] G. Kothleitner, W. Grogger, M. Dienstleder, and F. Hofer, Microsc. Microanal., doi: 10.1017/S1431927614000130 (2014).
[22] B. D. Forbes, A. V. Martin, S. D. Findlay, A. J. D'Alfonso, and L. J. Allen, Phys. Rev. B **82**, 104103 (2010).
[23] R. F. Egerton, *Electron Energy-loss Spectroscopy in the Electron Microscope* (Plenum Press, New York and London, 1996).
[24] P. D. Robb and A. J. Craven, Ultramicroscopy **109**, 61 (2008).
[25] N. R. Lugg, M. Haruta, M. J. Neish, S. D. Findlay, T. Mizoguchi, K. Kimoto, and L. J. Allen, Appl. Phys. Lett. **101**, 183112 (2012).
[26] M. J. Neish, N. R. Lugg, S. D. Findlay, M. Haruta, K. Kimoto, and L. J. Allen, Phys. Rev. B **88**, 115120 (2013).
[27] P. C. Hansen, *Discrete Inverse Problems* (Society for Industrial and Applied Mathematics, Philadelphia, 2010).